


## Laser stimulation of MoSe<sub>2</sub>/Au(111) in an STM junction: Photoinduced versus thermally induced current response

Björn Lübken and Niklas Nilius <sup>\*</sup>*Institute of Physics, Carl von Ossietzky University, 26111 Oldenburg, Germany*

(Received 2 March 2021; revised 28 May 2021; accepted 1 June 2021; published 15 June 2021)

A laser beam is focused onto the junction of a scanning tunneling microscope (STM) to probe the local photocurrent response of highly ordered MoSe<sub>2</sub> islands. The islands, grown by physical vapor deposition onto Au(111), are characterized by uniform triangular shapes, Mo-terminated edges, and the typical 1.8 V band gap of monolayer MoSe<sub>2</sub>. The laser-induced signals are detected with nanometer spatial resolution by a lock-in amplifier, both in the form of point spectra and surface maps. To distinguish real photocurrents from current contributions, arising from periodic tip expansions due to the dissipated laser power, blind experiments are performed in which the tip height is modulated without laser irradiation. In addition, the expected current responses are simulated as a function of sample bias for the two scenarios. Comparison between experimental and simulated data indicates that periodic tip expansions dominate the detected current modulations and photoinduced signals are of minor importance. Our work provides various indicators to safely distinguish photo- and thermally induced current components in a laser-driven STM experiment and discusses means to enhance the desired photoresponse with respect to parasitic thermal effects.

DOI: [10.1103/PhysRevB.103.245420](https://doi.org/10.1103/PhysRevB.103.245420)

### I. INTRODUCTION

Fundamental understanding of light-matter interactions is the basis of many technologically relevant processes in the fields of photovoltaics, optoelectronics, and quantum technologies. To connect structural peculiarities, such as point defects and grain boundaries, with a distinct optical response, surfaces need to be explored at atomic length scales. Scanning probe techniques, especially optical near-field and scanning tunneling microscopy (STM), can largely contribute to this topic, either by probing the local luminescence upon electronic stimulation or inducing photocurrents by shining light onto the tunneling junction [1–4].

First attempts to measure photocurrents at the nanoscale by STM date back to the 1990s and already dealt with the unique optical response of transition metal dichalcogenides (TMDCs) [5]. Experiments on bulk WSe<sub>2</sub> revealed a pronounced forward current under laser irradiation that was ascribed to a reduced surface band bending in presence of photogenerated electron-hole pairs. This interpretation was confirmed in later studies on WS<sub>2</sub>, where band pinning due to surface defects diminished the photoresponse [6]. STM experiments on molecular layers demonstrated the possibility to switch photocurrents from *p*- to *n*-type behavior [7,8]. On patterned semiconductors, a material contrast was detected in STM photocurrent maps and explained with local differences in the band gap and surface termination [9]. However, the high locality of the photoresponse was questioned in studies on Ag- and Au-modified Si(111) that did not reveal a respective contrast between the different surface regions [10].

Recent STM activities moved toward time-resolved photocurrent measurements and explored, for example, the

transient occupation of molecular orbitals and the dielectric screening in semiconductors [11,12]. However, laser-driven STM experiments are always hampered by the unknown impact of thermal tip expansion due to the laser irradiation. In fact, clear distinction between photo- and thermally induced currents turned out to be difficult, which renders data interpretation in those experiments challenging [13,14].

In this work, MoSe<sub>2</sub> islands grown on Au(111) are exposed to modulated laser light in order to induce local photocurrents in the STM junction. Our study is inspired by the fascinating optical properties of TMDC monolayers, as governed by the direct band gap and the spin-valley electronic structure [15–17]. The optical response of TMDCs is dominated by Wannier excitons confined in two dimensions. This gives rise to large binding energies and opens means to control the excitonic properties by changes of the dielectric environment [18,19]. Whereas the optical response of TMDC layers was comprehensively addressed in far-field experiments, STM was mainly used to probe their atomic structure, defect landscape, and electronic properties [20–22]. The TMDC luminescence was probed only in a few STM experiments [23–25] and just a single photocurrent study is reported to our best knowledge, yet with ambiguous results [26].

In this study, high-quality MoSe<sub>2</sub> islands are grown on Au(111) and analyzed with respect to their atomic structure and electronic properties. In addition, the current response upon shining laser light onto the STM junction is detected as a function of bias voltage and laser polarization. A number of control experiments and model calculations are undertaken to assign the detected current signals to either photo- or thermally induced effects. Our analyses find periodic tip expansions due to dissipated laser light to be the main source of the current response. Our work thus underlines the large susceptibility of laser-driven STM experiments to misinterpretations.

<sup>\*</sup>niklas.nilius@uni-oldenburg.de

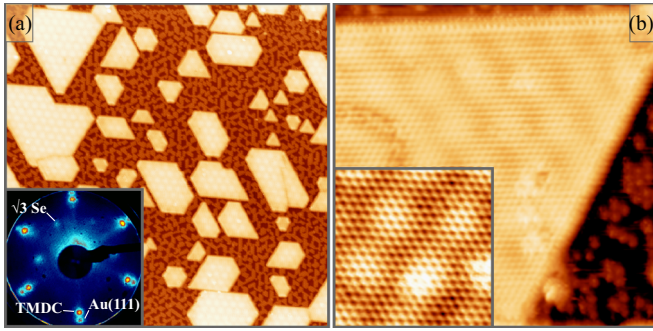


FIG. 1. (a) STM overview image of MoSe<sub>2</sub> islands on Au(111) ( $90 \times 90 \text{ nm}^2$ ,  $U_B = 1.0 \text{ V}$ ,  $I = 0.5 \text{ nA}$ ). Open Au patches around the islands are covered with a  $(\sqrt{3} \times \sqrt{3})R30^\circ$  superstructure of Se atoms. The inset shows a LEED pattern with distinct double spots, reflecting the two lattice periodicities ( $E_{\text{kin}} = 55 \text{ eV}$ ). (b) Atomically resolved STM image of an individual MoSe<sub>2</sub> island, showing the Mo sublattice and the moiré pattern ( $15 \times 15 \text{ nm}^2$ , inset  $5.5 \times 5.5 \text{ nm}^2$ ).

## II. EXPERIMENT

All experiments are performed with a custom-built Pan-type STM operated at liquid nitrogen temperature. The microscope is embedded in an ultrahigh-vacuum chamber ( $5 \times 10^{-10}$  mbar base pressure), equipped with the standard preparation and analysis tools of surface science. Electrochemically etched gold tips are used for imaging and spectroscopy. A diode laser with 1.95 eV photon energy and 1 mW power is employed for optical excitations. The associated current response is detected with lock-in technique by electronically modulating the laser intensity at 575 Hz. The laser beam is focused in a  $30^\circ$  angle with respect to the sample surface via a lens system and aligned by maximizing the associated current signal. A laser polarization along the tip-sample axis is used if not stated otherwise. While large thermal drifts corrupt the STM performance after laser ignition, stable imaging conditions are reached after 30 min of thermalization.

The TMDC islands are grown on an Au(111) single crystal, cleaned by repeated  $Ar^+$  sputtering and 800 K annealing cycles. The preparation involves simultaneous deposition of Mo and Se from two e-beam evaporators onto the substrate held at 400 K. To stimulate ordering of the TMDC, the sample is postannealed at 750 K, first in Se background and then in vacuum. Successful sample preparation is concluded from electron diffraction (LEED) data, showing two closely spaced hexagonal spot patterns in accordance with the 12% lattice mismatch between Au(111) and MoSe<sub>2</sub> (Fig. 1).

## III. RESULTS AND DISCUSSION

### A. Structure and morphology of the MoSe<sub>2</sub> islands

Figure 1(a) depicts an STM overview image of a characteristic sample. The MoSe<sub>2</sub> patches are readily identified by their triangular shape, being altered only if two adjacent islands coalesce to a rhombic geometry. Typical edge lengths vary between 80 and 200 Å. The island height is determined to be 2.5 Å, being smaller than the geometric height due to state-density differences with respect to gold.

The Au(111) surface around the TMDC is covered with Se atoms, arranged in a  $(\sqrt{3} \times \sqrt{3})R30^\circ$  superstructure in order to minimize short-range repulsive forces [27]. The presence of Se adatoms indicates a TMDC preparation in selenium excess. Figure 1(b) shows an ideal MoSe<sub>2</sub> triangle with atomic resolution. Apart from the Mo sublattice, a moiré pattern with 25 Å periodicity is seen, arising from the overlay of Au(111) and MoSe<sub>2</sub> lattices with 2.89 and 3.25 Å spacing, respectively. From this topographic data, the growth geometry of MoSe<sub>2</sub> is determined to be the 1H type, with interface and surface Se atoms sitting on top of each other [21]. The abundance of triangular over hexagonal islands demonstrates the energetic preference of Mo- with respect to Se-terminated edges, in agreement with earlier studies [28].

### B. Electronic properties

As electronic and optical properties are closely related, differential conductance ( $dI/dV$ ) spectroscopy was performed on the TMDC islands. Figure 2(a) presents a series of  $dI/dV$  spectra, taken at different positions within a MoSe<sub>2</sub> island. All spectra display the direct band gap at the  $K$  point of MoSe<sub>2</sub> that spans from the valence-band top at  $-1.25 \text{ V}$  to the bottom of the conduction band at  $+0.6 \text{ V}$  [22,29]. Two pronounced maxima appear at 1.1 and 1.6 V, marking the lower and upper conduction-band onset at the  $\Gamma$  point that are easily accessed by the tunneling electrons [22,30]. Similarly, a  $dI/dV$  shoulder at  $-1.6 \text{ V}$  reflects electron tunneling from the valence-band edge at the  $\Gamma$  point.

Conductance maps reveal the spatial localization of electronic states in the MoSe<sub>2</sub> islands [Fig. 2(b)]. At low positive bias, the TMDCs exhibit smaller intensity than the Au(111) (not shown). The contrast reverses at the conduction-band onset and the MoSe<sub>2</sub> appears bright at  $+1.0 \text{ V}$ . Also at negative polarity, the islands show up with dark contrast inside the gap region ( $-0.5 \text{ V}$ ). The contrast switch occurs, however, not at the  $K$ -point edge of the valence band, but only when tunneling from the  $\Gamma$  point sets in at  $-1.6 \text{ V}$  [30]. The MoSe<sub>2</sub> edges appear bright in  $dI/dV$  maps taken at  $-1.0$  and  $+1.8 \text{ V}$ . The underlying one-dimensional electronic states are localized along the Mo edges [28,31], and are also detected in the  $dI/dV$  spectra [see arrows in Fig. 2(a)].

### C. Laser-induced current signals

To detect a possible photoresponse of the MoSe<sub>2</sub> islands, current modulations are probed with a lock-in amplifier set to the chopping frequency of the laser. The detected signal is referred to as  $dI/dL$  ( $L$  for laser) in the following. Figure 3 depicts bias-dependent  $dI/dL$  maps of MoSe<sub>2</sub> islands and a corresponding STM image. In the topography, the TMDCs are readily identified by their triangular shape and bright contrast with respect to the Se/Au(111). In the  $dI/dL$  maps, they are best recognized with the help of their edges that always appear as dark lines. Moreover, open gold patches are often characterized by a fuzzy intensity distribution, as isolated Se atoms become mobile and swap binding sites upon laser irradiation.

The MoSe<sub>2</sub> islands undergo a distinct  $dI/dL$  contrast evolution as a function of sample bias. These contrast changes

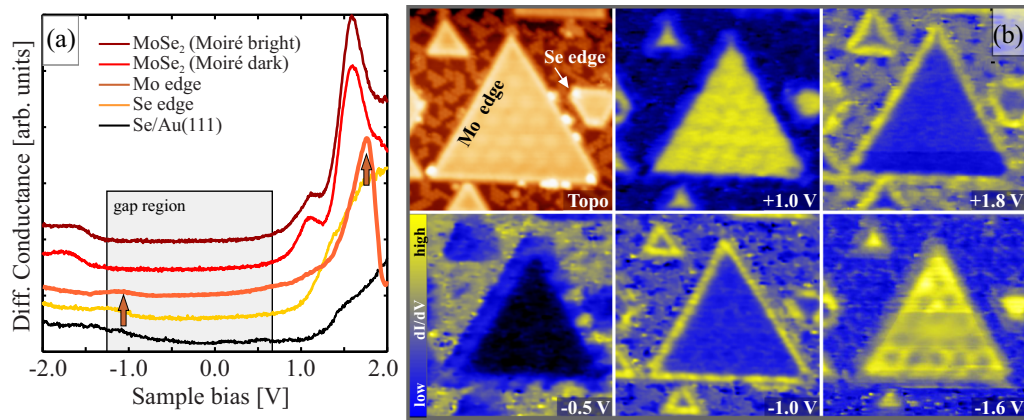


FIG. 2. (a) STM conductance spectra taken at different positions of a MoSe<sub>2</sub> island and the support (bias set point: 2.0 V). (b) STM topographic and conductance maps acquired at the indicated bias voltages (20 × 20 nm<sup>2</sup>, *I* = 1.0 nA). At −1.0 and +1.8 V, pronounced edge states are revealed, which are also marked by arrows in panel (a).

reflect the impact of bias voltage on both the accessible final states for photoexcited electrons and the tip-sample distance. At low positive bias, the entire surface appears with similar contrast apart from the dark edges [Fig. 3(a)]. A first change occurs at 2.0 V, when the Au surface gains intensity with respect to the TMDC. The contrast reverses at 3.0 V when the MoSe<sub>2</sub> islands turn bright. At 5.0 V finally, the TMDC islands appear black against a bright Se/Au(111) background. The contrast evolution at negative bias is rather monotonous. The MoSe<sub>2</sub> islands show up with similar intensity as the gold between −1.0 and −2.5 V, but develop slightly stronger *dI/dL* signals at more negative bias.

The overall intensity course derived from the *dI/dL* maps is depicted with red and black circles in Fig. 3(b). Apparently, larger differences only occur at 2.0 and above 3.0 V when the Se/Au(111) and the MoSe<sub>2</sub> regions exhibit higher *dI/dL* intensities, respectively. At negative polarity, the TMDCs show slightly larger signals as bias increases. Similar data are obtained in point spectra, being acquired by placing the tip atop a selected surface site and detecting the *dI/dL* signal during a bias ramp with enabled feedback loop [Fig. 3(b)]. Also here, the *dI/dL* signal of Se/Au(111) is larger at 2.0 V, but gets smaller than the TMDC intensity above 3.0 V. At negative polarity, the TMDC signal steadily gains intensity with respect

to that of Se/Au(111). Common for both polarities is a diminishing *dI/dL* signal with increasing bias voltage, whereby positive-bias values are generally higher than their negative counterparts.

The impact of laser polarization on the *dI/dL* signal is tested by turning the polarization direction from parallel to perpendicular to the tip-sample axis [Fig. 3(b)]. A parallel polarization, as used for the measurements in Fig. 3(a), consistently results in larger *dI/dL* signals than the orthogonal direction. This finding points to field-enhancement effects in the STM junction acting on the *dI/dL* intensity. A laser polarization along the tip-sample axis hereby drives coherent plasmon excitations in the electrodes, both made of gold with excellent plasmonic properties [3,32]. The resulting near-field enhancement would then promote the overall optical activity of the STM contact and amplify the *dI/dL* signal.

**D. Current signals due to tip height modulations**

Laser irradiation of an STM contact may stimulate photoassisted tunneling, but also trigger periodic changes of the tip height above the surface. The dissipated laser power hereby initiates tiny temperature fluctuations, causing the tip to elongate in sync with the chopping frequency. Although the

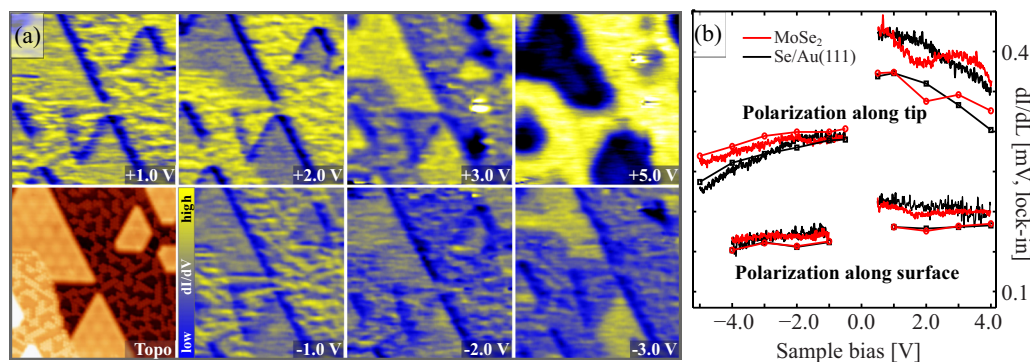


FIG. 3. (a) STM topography and corresponding *dI/dL* maps for selected bias voltages (25 × 25 nm<sup>2</sup>, *I* = 0.5 nA). (b) Bias-dependent *dI/dL* spectra (curves) and intensity values extracted from *dI/dL* maps (points) taken on MoSe<sub>2</sub> islands and Se/Au(111) patches. Larger *dI/dL* signals are detected for a laser polarization along the tip-sample axis.

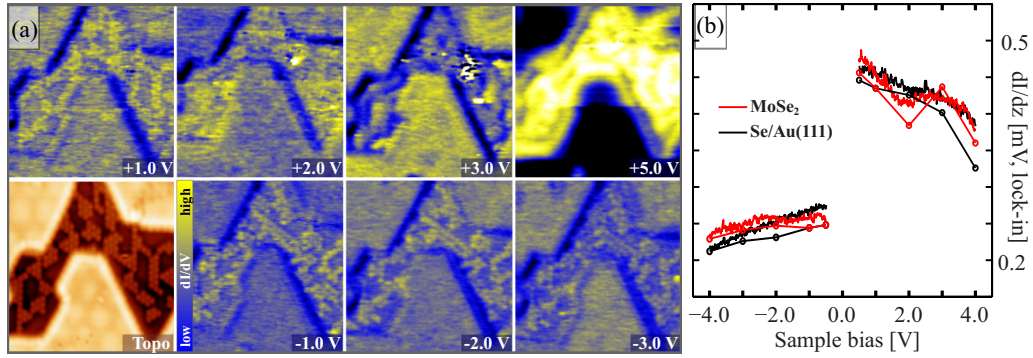


FIG. 4. (a) STM topography and  $dI/dz$  maps for selected bias voltages ( $25 \times 25 \text{ nm}^2$ ,  $I = 0.5 \text{ nA}$ ). (b) Corresponding  $dI/dz$  spectra (curves) and intensity values extracted from the maps (points) for tip positions above  $\text{MoSe}_2$  and  $\text{Se}/\text{Au}(111)$  surface regions.

effect is partly compensated by the feedback loop of the microscope, it may still induce current modulations to be mixed up with a photocurrent signal [13]. In a control experiment, we have mimicked such periodic height changes by adding a small sinusoidal bias to the tip piezo. The resulting AC current, referred to as  $dI/dz$  thereafter, was detected with lock-in technique. Comparable signal strength to the  $dI/dL$  response was hereby reached already for a  $z$  modulation of 5 pm.

Corresponding  $dI/dz$  maps of the  $\text{MoSe}_2/\text{Au}(111)$  surface were now acquired at identical conditions, except that the laser irradiation was replaced by a  $z$  modulation (Fig. 4). Several similarities to the laser-induced maps can be identified at first glance. The  $dI/dz$  signal undergoes a comparable bias evolution, yielding bright contrast of the  $\text{Se}/\text{Au}(111)$  patches at 2.0 V, higher  $\text{MoSe}_2$  intensity at 3.0 V, and a sharp drop of the TMDC signal at 5.0 V sample bias. Also, the tiny contrast changes between  $\text{MoSe}_2$  islands and  $\text{Se}/\text{Au}$  patches at negative polarity are well reproduced in the  $dI/dz$  channel. A more quantitative assessment is obtained by plotting the  $dI/dz$  signal, as extracted from maps in Fig. 4(a), as a function of bias voltage. The traces are additionally compared to  $dI/dz$  point spectra, acquired on selected  $\text{MoSe}_2/\text{Au}(111)$  surface regions. The analogy of bias-dependent  $dI/dL$  and  $dI/dz$  intensity courses is compelling. It suggests that an active  $z$  modulation of the tip height yields a current response that is similar to the one produced by exposing the STM to chopped laser light. However, it is unclear at this point whether the  $dI/dz$  signal only shows a bias behavior similar to the photocurrent, or thermal effects due to laser dissipation are indeed responsible for the  $dI/dL$  signal. To distinguish a true photocurrent from a parasitic thermal signal, both current components have been simulated, as discussed in the next paragraph.

### E. Modeling photo- and tip height induced currents in an STM

The different current components due to photoassisted tunneling and thermally induced tip-height changes are modeled with the Wenzel-Kramers-Brillouin approximation:  $I \sim \int dE \rho_{\text{sample}}(r_{\text{Tip}}, E) \rho_{\text{Tip}}(E - eV) T(z, E, V)$  [33]. Here,  $\rho_{\text{sample}}$  and  $\rho_{\text{Tip}}$  are the respective state densities and  $T(z, E, V) = \exp[-\frac{2z}{\hbar} \sqrt{2m(\varphi - E + \frac{1}{2}eV)}]$  is the effective barrier height, with  $z$  and  $V$  the tip-sample distance and the applied bias volt-

age, respectively. The work function  $\varphi$  is set to 5.0 eV, which is an average value between  $\text{Se}/\text{Au}(111)$  and  $\text{MoSe}_2/\text{Au}(111)$ . A simplified state density that includes the TMDC band gap at the  $\Gamma$  and  $K$  points and the  $\text{Au}(111)$  surface band above  $-0.5$  eV is used for the sample [34]. The state density of the tip is set constant, as it arises from the wide  $6sp$  band of gold. Only relative  $\rho_{\text{sample}}$  and  $\rho_{\text{Tip}}$  values are considered, as our focus lies on qualitative trends in the various current contributions.

In a first step, the tip-sample distance at constant current is calculated as a function of bias voltage, as shown by the filled symbols in Fig. 5(a). Independent of the polarity, the tip quickly retracts from the surface as the bias increases from zero, reflecting the additional number of transport channels that contribute to the tunneling current. Above 2 V, the tip electric field becomes the decisive parameter and causes the tunneling gap to increase almost linearly with bias

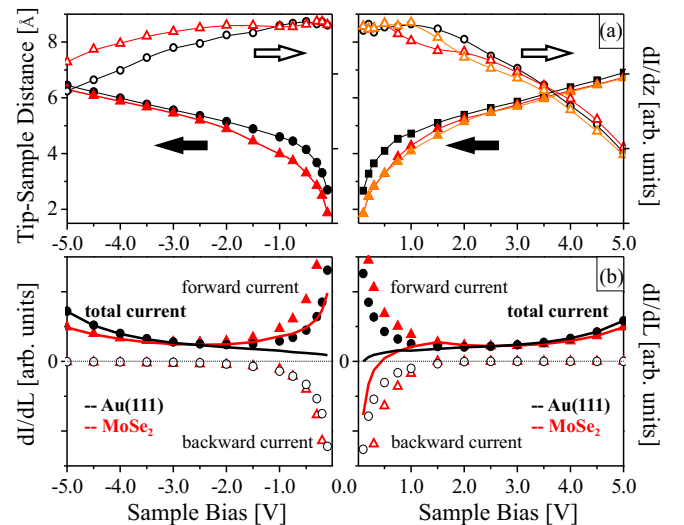


FIG. 5. (a) Tip-sample distance (filled symbols) and  $dI/dz$  signal (open symbols) calculated as a function of bias voltage for an STM junction comprising an Au tip and a  $\text{MoSe}_2/\text{Au}(111)$  or bare  $\text{Au}(111)$  surface. The red and orange curves consider the  $K$ - and  $\Gamma$ -point gap in the TMDC bands, respectively. (b) Simulated photocurrents in the same STM contacts at negative and positive polarity. Forward and backward photocurrents are depicted by filled and empty symbols, respectively; the total current is marked by solid lines.

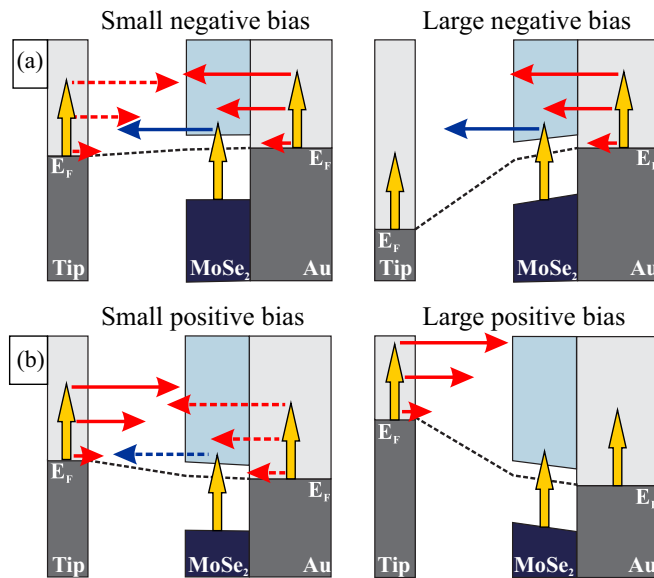


FIG. 6. Potential diagram of an STM junction comprising a gold tip and a MoSe<sub>2</sub>/Au(111) sample at (a) negative and (b) positive bias. Photoexcitations of electrons in tip and sample (yellow arrows) induce forward and backward photocurrents, as depicted by solid and broken arrows, respectively. While photocurrents from the MoSe<sub>2</sub> are shown with blue color, the ones originating from the gold are depicted in red.

voltage (Fowler-Nordheim limit). Although the general distance behavior is comparable for MoSe<sub>2</sub> and Au(111), small deviations can be observed. The MoSe<sub>2</sub> band gap leads to a reduced tunneling gap below  $\pm 1.5$  V, while the Shockley surface band gives rise to a particularly steep distance-bias curve between the band onset and +1.0 V for Au(111).

Based on these distance curves, the  $dI/dz$  signal is evaluated next. For this purpose, changes in the tunneling current due to tip-height modulations are calculated, as depicted by the open symbols in Fig. 5(a). The  $dI/dz$  curves are relatively flat at low bias, reflecting the balance between the opening of new tunneling channels and the rising tip-sample distance, but decline more steeply at higher bias. Moreover, the onset of the MoSe<sub>2</sub> conduction band becomes manifest by a slight decrease of the  $dI/dz$  intensity, being caused by the availability of additional electron transport channels. The red and orange curves hereby depict the cases in which either the small  $K$ -point gap (red) or the larger  $\Gamma$  gap (orange) of MoSe<sub>2</sub> have been used in the calculations. At negative bias, the lower state density of the TMDC is responsible for a slightly reduced slope of the  $dI/dz$  curves.

The  $dI/dL$  signal, on the other hand, accounts for the tunneling of photoexcited electrons between tip and sample. Given their high energy above the Fermi level,  $E_F$ , the hot electrons experience a lower tunneling barrier than the equilibrium carriers in the junction [35]. The tip-sample distance for the process was adopted from the conventional STM current simulations discussed above. The stimulation of electrons takes place in both tip and sample and covers an energy window from  $E_F$  to  $E_F + \hbar\omega$ , whereby  $\hbar\omega = 1.95$  eV is the laser energy (Fig. 6). The total photocurrent thus comprises a forward and backward component, with the former one running

parallel to the DC current of the junction. The photoexcitation process itself is not accounted for and all transition matrix elements have been set equal. This necessarily disregards the role of the direct band gap and of excitonic modes in the MoSe<sub>2</sub> monolayer for the optical response. Also, direct photoemission is neglected in our model, as the laser energy is well below the work function of the STM electrodes.

The results of our photocurrent simulations are compiled in Fig. 5(b) and first discussed for negative polarity when the DC current flows from the sample to the tip. At low bias, large photocurrents start from both electrodes, as the hot carriers easily find empty states on the other side of the gap [Fig. 6(a)]. Whereas on Au(111), the forward and backward photocurrent nearly cancel out, the forward current exceeds the backward component on MoSe<sub>2</sub>. The reason is efficient tunneling of photocarriers from the bottom of the TMDC conduction band into the tip. At more negative bias, the backward photocurrent from the tip ceases, as hot electrons cannot find empty states for tunneling anymore. The consequence is a continuous rise of the total photocurrent. The effect gets further enhanced as the tunneling barrier decreases faster for photoexcited than equilibrium carriers, while the latter were used to compute the tip-sample distance. At the chosen state densities for tip and sample, the total photocurrent increases more on pure Au(111) than TMDC-covered surfaces, although this trend is not reliably predicted by our simulation.

The behavior is mirrored at positive polarity, when the DC current flows from the tip to the sample [Fig. 5(b)]. On Au(111) patches, forward and backward photocurrents nearly compensate at low bias and the total photocurrent is small. It rises continuously at higher bias, as the backward photocurrent terminates and the photoelectrons in the forward direction experience a decreasing tunneling barrier [Fig. 6(b)]. Above the MoSe<sub>2</sub>, the backward photocurrent exceeds the forward component at low bias and the total photocurrent flows in opposite direction to the DC current of the STM. With increasing bias, the backward component declines while forward electrons from the tip benefit from a diminishing tunneling barrier, causing the total photocurrent to reverse its direction. The competition of the two contributions gives rise to a shallow photocurrent maximum on the TMDC patches that depends, however, on the exact state densities employed in the calculations.

Our simulations provide qualitative insights into the bias dependence of the different current contributions in a laser-assisted STM experiment. While the thermally induced component, i.e., the  $dI/dz$  signal, continuously decreases with bias voltage, the  $dI/dL$  signal follows the opposite trend. A comparison of experiment and simulation should therefore allow us to safely differentiate thermally and photoinduced effects in an STM junction.

## F. Comparison of experimental and simulated current traces

Remember that the  $dI/dL$  and  $dI/dz$  spectra, acquired by laser irradiation and periodic tip-height modulations in the STM junction, respectively, exhibit a rather similar bias-dependent behavior (Figs. 3 and 4). Already a rough comparison with our simulations reveals that the experimental curves closely follow the calculated  $dI/dz$  response. The

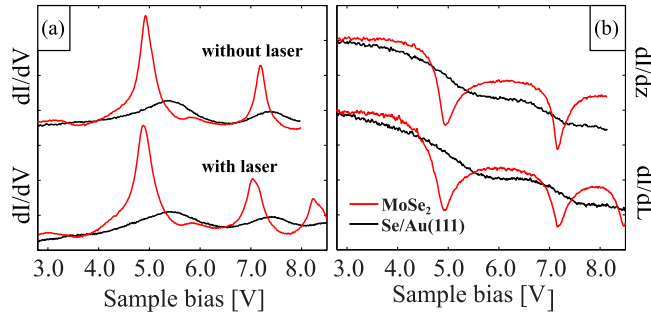


FIG. 7. (a) Differential conductance spectra of  $\text{MoSe}_2/\text{Au}(111)$  samples measured without (top) and with laser irradiation (bottom). (b) Associated  $dI/dz$  spectra acquired by modulating the tip height (top) and  $dI/dL$  spectra measured with laser irradiation (bottom). All spectra were taken with enabled feedback loop and clearly display the FERs. No shift of the resonance positions is detected in response to the laser irradiation.

measured AC current seems therefore triggered by periodic tip expansions due to the dissipated laser power, while the expected signature of a photocurrent is not observed. Even details in the measured  $dI/dL$  and  $dI/dz$  traces can be matched with the simulations. Spectra of the  $\text{MoSe}_2$  islands consistently show a dip at 2.0 V that is absent on the  $\text{Se}/\text{Au}(111)$ . A similar dip in the simulated  $dI/dz$  behavior has been assigned to the sudden increase of the current response when reaching the TMDC conduction band. Its bias position even indicates that the band onset at the  $\Gamma$  point and not the smaller  $K$  gap of  $\text{MoSe}_2$  is responsible for the  $dI/dz$  dip [Fig. 5(a), red versus orange lines]. A similar spectral feature is not observed in the calculated  $dI/dL$  response. The  $dI/dz$  minimum at 2.0 V also explains the contrast inversion of the  $\text{MoSe}_2$  islands in the experimental maps (Figs. 3 and 4). At this bias, the TMDCs appear with reduced intensity as compared to  $\text{Se}/\text{Au}(111)$  that does not exhibit a discontinuity in the  $z$ -induced current response.

The assignment of the laser-induced current signal to a thermal effect can be independently confirmed with the help of high-bias spectra taken on the  $\text{MoSe}_2/\text{Au}(111)$  surface. At bias voltages above the sample work function, tip electrons leave the classically forbidden tunneling barrier and propagate as free carriers through the junction [36]. If multiples of their half wavelength match the dimension of the vacuum gap between tip and sample, electrons are caught in bound vacuum states, the so-called field emission resonances (FERs). Given their high transmission probability for electrons, the FERs show up as pronounced maxima in the differential conductance [37]. The FERs are readily detected in our spectra, whereby the series of maxima starts earlier and is more pronounced on the  $\text{MoSe}_2$  islands than on the surrounding  $\text{Se}/\text{Au}(111)$  [Fig. 7(a), upper curves]. Reasons for this are the absent electron spill-out and the smaller surface dipole on the dielectric TMDCs in combination with the high electronegativity of the Se atoms bound to the pristine gold [38].

Photoexcited electrons are now expected to reach the FER states at lower bias, as their starting position in the tip bands is upshifted by the energy of the absorbed photons. In

earlier experiments, such shifts of the FERs have indeed been observed upon exposing the STM junction to laser light, whereby changes in the bias position exactly matched the photon energy [39]. In contrast, no shift of the FERs is detected here, and  $dI/dV$  curves taken under dark and illuminated conditions feature the same resonance energies [Fig. 7(a)]. Also, the associated  $dI/dL$  spectra show a similar behavior, except that the resonances are mirrored along the  $x$  axis [Fig. 7(b), bottom]. This phase shift with respect to the  $dI/dV$  curves can be understood by assuming a thermal instead of a photoinduced origin of the signal. Running through a series of FERs results in a stepwise retraction of the tip from the surface [37]. This backward motion is required to maintain the preset tunneling current when a new FER, i.e., new and effective transport channel for electrons, is reached. The  $dI/dL$  signal that actually reflects a thermal response follows this trend in a differential manner; i.e., the signal runs through a negative resonance as the tip takes a backward step. Exactly the same behavior is seen if a finite tip modulation replaces the laser irradiation [Fig. 7(b), top]. This identity of  $dI/dz$  and  $dI/dL$  curves would not be expected for a spectral response produced by photoexcited electrons in the junction. The position of the FERs thus provides another means to discriminate between photo- and thermal effects in an STM.

The last paragraph addresses the confusing dependency of the detected  $dI/dL$  signal on the laser polarization. Larger  $dI/dL$  intensities were found for a polarization direction along the tip-sample axis [Fig. 3(b)], which seems compatible with photoinduced processes promoted by field-enhancement effects in the STM [32]. Conversely, tip expansion due to dissipated laser power should be independent of the polarization at first glance. However, this picture is too simple. Light absorption and the subsequent thermal effects are largely controlled by plasmon excitations in the gold tip used in our experiments. Two plasmon modes are of relevance at the very tip apex [40]. While modes along the tip axes have low energy, the perpendicular ones are considerably blueshifted given their confinement in the tip diameter. For a polarization direction along the tip, the red laser of our experiment preferentially couples to the energy-matched on-axis plasmons. The orthogonal modes with higher energy, on the other hand, are not excited even for perpendicular laser polarization. As a consequence, less power is dissipated and smaller tip-height modulations are induced in this geometry, in agreement with the observations. In general, the laser polarization seems an inadequate parameter to distinguish photo- from thermally induced current contributions in the STM junction.

#### IV. CONCLUSIONS

Shining a focused laser beam onto  $\text{MoSe}_2/\text{Au}(111)$  islands in an STM contact was found to produce a strong AC current and a pronounced bias-dependent contrast in the respective  $dI/dL$  maps. Disturbingly, a similar current response was revealed by adding a sinusoidal modulation to the tip height ( $dI/dz$ ), in order to mimic periodic tip expansions. A comparison of the experimental  $dI/dL$  and  $dI/dz$  spectra with simulated photo- and height-related tunneling signals confirms that laser irradiation of the STM junction is mainly responsible for thermal effects in the tunneling gap.

The following strategies shall be tested to overcome this dilemma in future experiments. First, photo- and thermally induced currents in an STM gap are known to obey different frequency schemes [14]. While the photoresponse is essentially instantaneous and mainly limited by the bandwidth of the current amplifier, thermal effects are relatively slow. Increasing the chopping frequency of the laser toward the MHz regime thus helps to suppress parasitic AC currents due to thermal effects. Second, an anticyclical excitation sequence of an in-

frared and a visible-light laser might be employed to keep the thermal load of the STM junction constant, while generating a modulated photocurrent signal to be detected with the lock-in technique. Respective experiments are presently on the way.

#### ACKNOWLEDGMENT

Financial support from DFG Grant No. Ni 650-5 is gratefully acknowledged.

- 
- [1] L. Novotny and S. J. Stranick, *Annu. Rev. Phys. Chem.* **57**, 303 (2006).
- [2] A. Hartschuh, *Angew. Chem., Int. Ed.* **47**, 8178 (2008).
- [3] R. Berndt, J. K. Gimzewski, and P. Johansson, *Phys. Rev. Lett.* **67**, 3796 (1991).
- [4] F. Rossel, M. Pivetta, and W. D. Schneider, *Surf. Sci. Rep.* **65**, 129 (2010).
- [5] F. R. F. Fan and A. J. Bard, *J. Phys. Chem.* **97**, 1431 (1993).
- [6] C. Ballif, M. Regula, and F. Levy, *Sol. Energy Mater. Sol. Cells* **57**, 189 (1999).
- [7] D. Fichou, F. Charra, and A. O. Gusev, *Adv. Mater.* **13**, 555 (2001).
- [8] A. Vezzoli, R. J. Brooke, S. J. Higgins, W. Schwarzacher, and R. J. Nichols, *Nano Lett.* **17**, 6702 (2017).
- [9] T. Takahashi, K. Takada, and M. Takeuchi, *Ultramicroscopy* **97**, 1 (2003).
- [10] K. Sell, I. Barke, S. Polei, C. Schumann, V. von Oeynhausen, and K. H. Meiwes-Broer, *Phys. Status Solidi B* **247**, 1087 (2010).
- [11] T. L. Cocker, D. Peller, P. Yu, J. Repp, and R. Huber, *Nature* **539**, 263 (2016).
- [12] V. Jelic, K. Iwaszczuk, P. H. Nguyen, C. Rathje, G. J. Hornig, H. M. Sharum, J. R. Hoffman, M. R. Freeman, and F. A. Hegmann, *Nat. Phys.* **13**, 591 (2017).
- [13] V. Gerstner, A. Thon, and W. Pfeiffer, *J. Appl. Phys.* **87**, 2574 (2000).
- [14] N. Naruse, Y. Mera, Y. Hayashida, and K. Maeda, *Ultramicroscopy* **107**, 568 (2007).
- [15] K. F. Mak, C. Lee, J. Hone, J. Shan, and T. F. Heinz, *Phys. Rev. Lett.* **105**, 136805 (2010).
- [16] D. Xiao, G.-B. Liu, W. Feng, X. Xu, and W. Yao, *Phys. Rev. Lett.* **108**, 196802 (2012).
- [17] Q. H. Wang, K. Kalantar-Zadeh, A. Kis, J. N. Coleman, and M. S. Strano, *Nat. Nanotechnol.* **7**, 699 (2012).
- [18] A. Raja, A. Chaves, J. Yu, G. Arefe, H. M. Hill, A. F. Rigosi, T. C. Berkelbach, P. Nagler, C. Schüller, T. Korn, C. Nuckolls, J. Hone, L. E. Brus, T. F. Heinz, D. R. Reichman, and A. Chernikov, *Nat. Commun.* **8**, 15251 (2017).
- [19] T. Cheiwchanchamnangij and W. R. L. Lambrecht, *Phys. Rev. B* **85**, 205302 (2012).
- [20] S. Helveg, J. V. Lauritsen, E. Lægsgaard, I. Stensgaard, J. K. Nørskov, B. S. Clausen, H. Topsøe, and F. Besenbacher, *Phys. Rev. Lett.* **84**, 951 (2000).
- [21] F. Cheng, Z. Hu, H. Xu, Y. Shao, J. Su, Z. Chen, W. Ji, and K. P. Loh, *ACS Nano* **13**, 2316 (2019).
- [22] A. J. Bradley, M. M. Ugeda, F. H. da Jornada, D. Y. Qiu, W. Ruan, Y. Zhang, S. Wickenburg, A. Riss, J. Lu, S.-K. Mo, Z. Hussain, Z.-X. Shen, S. G. Louie, and M. F. Crommie, *Nano Lett.* **15**, 2594 (2015).
- [23] N. Krane, C. Lotze, J. M. Läger, G. Reece, and K. J. Franke, *Nano Lett.* **16**, 5163 (2016).
- [24] D. Pommier, R. Bretel, L. Parra López, F. Fabre, A. Mayne, E. Boer-Duchemin, G. Dujardin, G. Schull, S. Berciaud, and E. Le Moal, *Phys. Rev. Lett.* **123**, 027402 (2019).
- [25] R. Péchou, S. Jia, J. Rigor, O. Guillemet, G. Seine, J. Lou, N. Large, A. Mlayah, and R. Coratger, *ACS Photonics* **7**, 3061 (2020).
- [26] H. Liu, Y. Li, M. Xiang, H. Zeng, and X. Shao, *ACS Nano* **13**, 6083 (2019).
- [27] J. Jia, A. Bendounan, H. M. N. Kotresh, K. Chaouchi, F. Sirotti, S. Sampath, and V. A. Esaulov, *J. Phys. Chem. C* **117**, 9835 (2013).
- [28] J. Lu, D. L. Bao, K. Qian, S. Zhang, H. Chen, X. Lin, S. X. Du, and H. J. Gao, *ACS Nano* **11**, 1689 (2017).
- [29] M. Yankowitz, D. McKenzie, and B. J. LeRoy, *Phys. Rev. Lett.* **115**, 136803 (2015).
- [30] N. Krane, C. Lotze, and K. J. Franke, *Surf. Sci.* **678**, 136 (2018).
- [31] M. V. Bollinger, J. V. Lauritsen, K. W. Jacobsen, J. K. Nørskov, S. Helveg, and F. Besenbacher, *Phys. Rev. Lett.* **87**, 196803 (2001).
- [32] P. Johansson and R. Monreal, *Z. Phys. B* **84**, 269 (1992).
- [33] C. Chen, *Introduction to Scanning Tunneling Microscopy* (University Press, Oxford, (2008).
- [34] G. Nicolay, F. Reinert, S. Hüfner, and P. Blaha, *Phys. Rev. B* **65**, 033407 (2001).
- [35] B. Schröder, O. Bunjes, L. Wimmer, K. Kaiser, G. A. Traeger, T. Kotzot, C. Ropers, and M. Wenderoth, *New J. Phys.* **22**, 033047 (2020).
- [36] O. Y. Kolesnychenko, Y. A. Kolesnichenko, O. I. Shklyarevskii, and H. van Kempen, *Phys. B (Amsterdam, Neth.)* **291**, 246 (2000).
- [37] E. D. L. Rienks, N. Nilis, H. P. Rust, and H.-J. Freund, *Phys. Rev. B* **71**, 241404(R) (2005).
- [38] L. Giordano, F. Cinquini, and G. Pacchioni, *Phys. Rev. B* **73**, 045414 (2006).
- [39] S. Liu, M. Wolf, and T. Kumagai, *Phys. Rev. Lett.* **121**, 226802 (2018).
- [40] U. Kreibig and W. Vollmer, *Optical Properties of Metal Clusters* Springer Series Materials Science, Vol. 25 (Springer, Berlin, (1995).